Functional and Structural Characterization of a Novel Anti-His-tag Antibody, HisMab-1

Natsuki Hitomi [1,†], Satowa Hoshi [2,†], Mika K. Kaneko [3], Ryuichi Kato [4], Kenji Iwasaki [2,5], Junichi Takagi [1], Yukinari Kato [3], Ayaka Harada-Hikita [2,5,*], and Takao Arimori [1,*]

*1 - **Laboratory for Protein Synthesis and Expression,** Institute for Protein Research, The University of Osaka, 3-2, Yamadaoka, Suita, Osaka 565-0871, Japan*

*2 - **Life Science Center for Survival Dynamics,** Tsukuba Advanced Research Alliance (TARA), University of Tsukuba, 1-1-1 Tennodai, Tsukuba, Ibaraki 305-8577, Japan*

*3 - **Department of Antibody Drug Development,** Tohoku University Graduate School of Medicine, 2-1, Seiryo-machi, Aoba-ku, Sendai, Miyagi 980-8575, Japan*

*4 - **Structural Biology Research Center,** Institute of Materials Structure Science, High Energy Accelerator Research Organization (KEK), 1-1 Oho, Tsukuba, Ibaraki 305-0801, Japan*

*5 - **Center for Quantum and Information Life Sciences (QiLS),** University of Tsukuba, 1-1-1 Tennodai, Tsukuba, Ibaraki 305-8577, Japan*

Correspondence to Ayaka Harada-Hikita and Takao Arimori: Life Science Center for Survival Dynamics, Tsukuba Advanced Research Alliance (TARA), University of Tsukuba, 1-1-1 Tennodai, Tsukuba, Ibaraki, 305-8577, Japan (A. Harada-Hikita). Laboratory for Protein Synthesis and Expression, Institute for Protein Research, The University of Osaka, 3-2, Yamadaoka, Suita, Osaka 565-0871, Japan (T. Arimori). *a-harada@tara.tsukuba.ac.jp (A. Harada-Hikita), arimori@protein.osaka-u.ac.jp (T. Arimori)*

https://doi.org/10.1016/j.jmb.2025.169574

Edited by Richard W. Kriwacki

Abstract

The polyhistidine tag (His-tag) is one of the most widely used peptide tags for the purification of recombinant proteins, owing to its compatibility with immobilized metal affinity chromatography. While numerous anti-His-tag antibodies are commercially available, their quantitative affinity data and structural insights are limited. Here, we present a detailed physicochemical and structural characterization of a novel anti-His-tag antibody, HisMab-1. Isothermal titration calorimetry showed that the Fab fragment of HisMab-1 binds to a hexahistidine peptide in an enthalpy-driven manner, with a dissociation constant (K_D) of ~30 nM at a neutral pH. The crystal structure of the HisMab-1–hexahistidine peptide complex at 2.39-Å resolution revealed that HisMab-1 primarily recognizes the first, second, fourth, and fifth histidine residues of the peptide through multiple interactions, including hydrogen bonding and π–π stacking, which collectively contribute to the high specificity of the antibody. Notably, HisMab-1 also binds to a His-tag embedded within a conformationally constrained β-hairpin loop without reducing affinity, highlighting its structural adaptability. These findings establish HisMab-1 as a high-affinity, high-specificity, structurally validated anti-His-tag antibody with broad potential in diverse protein engineering and structural biology applications.

Introduction

Tag systems have become indispensable tools in contemporary life science research, as they significantly facilitate the detection, visualization, and purification of recombinant proteins [1]. Various types of tags have been developed and utilized extensively in diverse experimental applications. Protein tags incorporating folded domains, such as glutathione S-transferase (GST, 26 kDa) and maltose binding protein (MBP, 42 kDa), enable purification of target proteins through their specific ligand-binding capabilities [2–5]. Additionally, these tags are sometimes used to improve the solubility of target proteins [6–10]. However, owing to their large molecular weight, they can affect the function of the fused protein. In contrast, short peptide tags exert minimal influence on the function of the target molecule. Epitope tags, including the FLAG-tag (DYKDDDDK; 8 residues) [11], MAP-tag (GDGMVPPG; 8 residues) [12,13], HA-tag (YPYDVPDYA; 9 residues) [14], c-Myc-tag (EQKLISEEDL; 10 residues) [15], and PA-tag (GVAMPGAEDDVV; 12 residues) [16], are used in combination with monoclonal antibodies (mAbs) that recognize these tag sequences. The high specificity and affinity of antibodies for their corresponding antigens facilitate the sensitive detection of epitope-tagged proteins, enabling their single-step purification with high purity through immunoaffinity chromatography (IAC) using antibody-immobilized resins. In IAC, the target molecule captured by the resin is typically eluted using a buffer containing a competitive peptide corresponding to the tag sequence.

Another peptide tag, the polyhistidine tag (His-tag), consisting of 6 to 10 consecutive histidine residues, which is among the most prevalent tags for recombinant protein purification [17]. The His-tag chelates with divalent metal ions such as Ni^{2+} and Co^{2+} immobilized on a resin, allowing the target protein to be captured on the resin. His-tagged proteins retained on the column can be eluted using a high concentration of imidazole or a low-pH buffer. This purification method, known as immobilized metal affinity chromatography (IMAC), is generally much more cost-effective than IAC because it does not require antibodies or synthetic peptides. Furthermore, as the interaction between metal ions and the His-tag does not require a specific conformation of the tag, it remains stable even in the presence of 6 M guanidine or 8 M urea. Therefore, IMAC is frequently employed under denaturing conditions as an initial step in the refolding process of recombinant proteins [18].

Although IMAC may be enough to purify a His-tagged protein, anti-His-tag antibody is still indispensable tool because it can be used to detect the target protein in techniques such as western blotting, flow cytometry, and enzyme-linked immunosorbent assay (ELISA). Several mAbs against the His-tag have been developed and are commercially available in various formats, including those labeled with fluorescent dyes or horseradish peroxidase (HRP). However, most of these mAbs have not been thoroughly characterized in terms of their affinity for the His-tag or their recognition mechanisms. Thus, appropriate data for these mAbs have not been sufficiently provided to users. Despite the importance of structural information in understanding how these antibodies recognize the His-tag, only one structural study of an anti-His-tag antibody has been reported to date [19]. In that study, Kaufmann et al. determined the crystal structure of the anti-His-tag antibody 3D5 in complex with a hexahistidine peptide. They revealed that its binding to the His-tag requires the three C-terminal histidine residues, including the terminal carboxyl group, thereby providing crucial information for the proper application of 3D5.

Recently, we established a novel anti-His-tag antibody, HisMab-1 (mouse IgG2b, κ) [20]. We found that HisMab-1 can bind not only to His-tags fused to the N- or C-terminus of the target molecule, but also to His-tags inserted into exposed loop regions of proteins. Leveraging this distinctive binding property, we have developed a unique epitope mapping method "HisMAP", where the reactivity of certain mAb against a series of 5 × His insertion variants of the antigen protein is screened with the HisMab-1 reactivity serving as a reference [20]. In the current study, we performed a detailed investigation of the binding properties of HisMab-1 to His-tags with various designs and positional configurations using surface plasmon resonance (SPR), ELISA, and isothermal titration calorimetry (ITC). We also determined the crystal structures of HisMab-1 in both the apo and peptide-bound forms. Based on these binding analyses and structural insights, we found that HisMab-1 possesses six histidine-binding pockets in its antigen-binding site, with the first, second, fourth, and fifth pockets playing particularly important roles in tag recognition. In addition, we demonstrated that HisMab-1 is capable of binding to a His-tag inserted into a highly constrained β-hairpin structure. These findings highlight the versatility and structural robustness of HisMab-1, positioning it as a valuable tool for detecting and analyzing His-tagged proteins in various contexts.

Results

Evaluation of HisMab-1 binding to variously designed His-tags

As His-tags consist of consecutive histidine residues, it is theoretically expected that longer tags provide more antibody binding sites and would exhibit higher apparent affinity. In the practical application, however, shorter tags are preferable to minimize potential impacts on the

target molecule. To determine the minimum number of histidine residues required for HisMab-1 binding, we evaluated its interaction with His-tags of various lengths. To this end, we attached a 3- to 6-residue His-tag to the C-terminus of the extracellular domain of angiotensin converting enzyme II (ACE2) as a model protein. To minimize steric hindrance from ACE2 during HisMab-1 binding to the His-tag, we inserted a 12-residue PA-tag as a spacer between ACE2 and the His-tag (Figure 1a and Supplementary Figure S1). The PA-tag can also serve as an independent detection and purification handle. We expressed ACE2-PA fused with four different lengths of His-tags, as well as ACE2-PA without a His-tag, in Expi293F cells, and purified them using Sepharose-immobilized anti-PA-tag antibody NZ-1 (K_D: 0.40 nM). These samples were flowed at various concentrations over a sensor chip immobilized with HisMab-1 and analyzed by SPR (Figure 1b). As a result, no binding response was detected with ACE2 containing 0, 3, and 4-residue His, whereas a significant response was detected for ACE2-5×His, and an even stronger response was observed for ACE2-6×His. We attempted to perform kinetic analysis using these sensorgrams; however, the sensorgrams did not fit well to the theoretical curves under any binding model tested, including 1:1 binding and two-state reaction models, and thus reliable K_D values could not be obtained. This was likely due to the presence of multiple binding modes arising from the consecutive histidine residues, which can bind to the antigen-binding pocket of HisMab-1 at slightly shifted positions.

Next, we investigated the number of histidine residues required to achieve sufficient performance in practical applications. ACE2-PA constructs with His-tags of various lengths were again expressed in Expi293F cells, and the culture supernatants were subjected to pull-down assays using resin immobilized with either HisMab-1 or

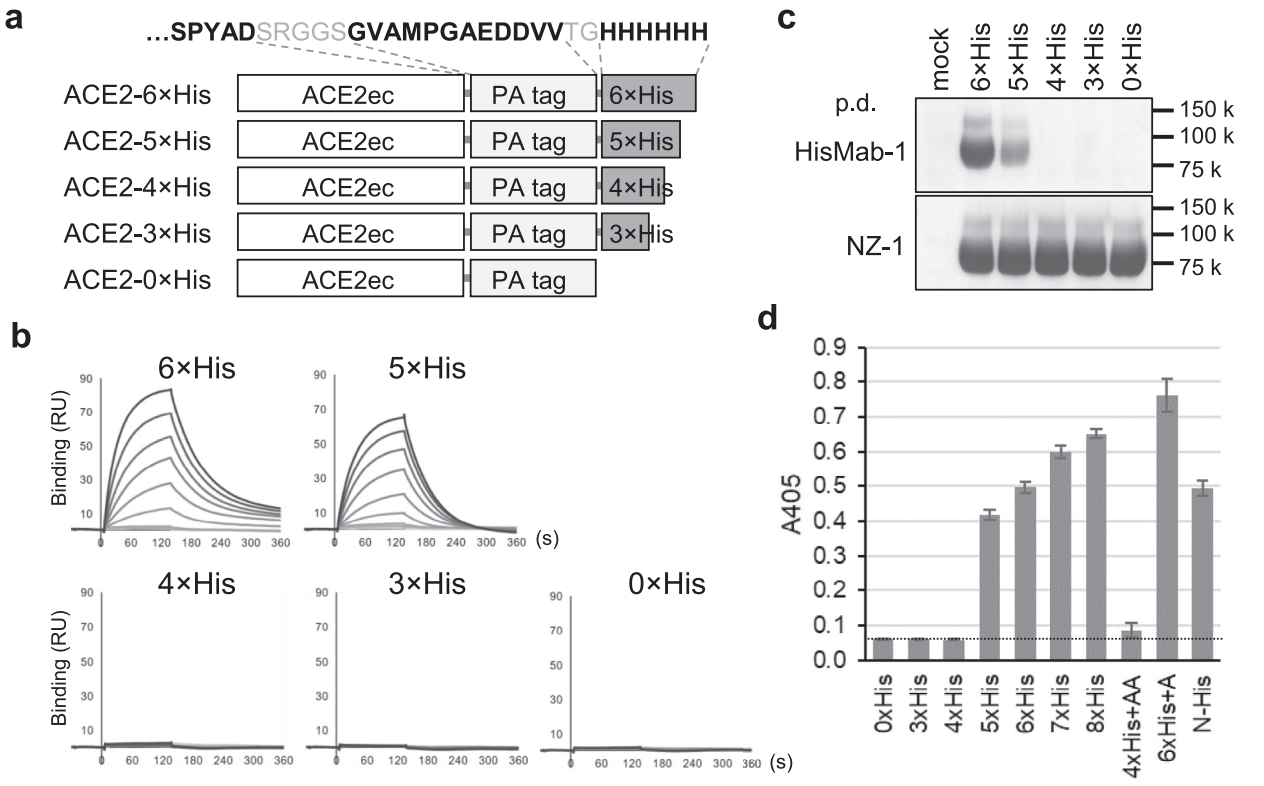

Figure 1. Binding analysis of HisMab-1 to His-tagged proteins with various designs. (a) Design of ACE2ec with a PA-tag and His-tags of various lengths. The amino acid sequence of the C-terminal tag region of ACE2-6×His is shown above. (b) SPR analysis. Binding curves obtained with different concentrations (1, 2, 4, 8, 16, 32, 64, 128, 256, 512, 1024, 2048 nM) of each ACE2ec sample were overlaid. (c) Pull-down assay. ACE2ec samples with His-tags of various lengths were expressed in Expi293F cells, precipitated with either HisMab-1- or NZ-1-immobilized resin, and analyzed by 12.5% SDS–PAGE under non-reducing conditions followed by Coomassie Brilliant Blue (CBB) staining. (d) Evaluation of HisMab-1 reactivity toward various His-tagged ACE2-PA proteins by ELISA. His-tagged ACE2-PA proteins were coated onto an immune plate and incubated with 10 nM HisMab-1. Antibody binding was detected using an HRP-conjugated antibody by measuring absorbance at 405 nm. A dotted line indicates the A_{405} value of the negative control (0×His). Data represent the mean ± SEM of three independent experiments.

NZ-1 (Figure 1c). In the pull-down assay using NZ-1, all samples showed comparable band intensities, confirming their equivalent expression levels. In contrast, in the assay using HisMab-1, no bands were observed for ACE2-3×His and ACE2-4×His, consistent with the results of the above SPR analysis. A band was detected for ACE2-5×His, but it was evident that not all of the expressed protein was captured. On the other hand, for ACE2-6×His, the band intensity was comparable to that observed with the NZ-1 resin, suggesting that most of the expressed ACE2-6×His was successfully captured. These results indicate that a 5-residue His-tag is the minimum length required for binding by HisMab-1, and that a 6-residue His-tag is practically sufficient.

Finally, we examined the binding properties of HisMab-1 toward longer His-tags and those containing non-histidine residues adjacent to the tag. Specifically, additional ACE2-PA constructs carrying C-terminal 7 × His, 8 × His, 4 × His plus two alanine residues (4×His+AA), 6 × His plus one alanine residue (6×His+A), or N-terminal 6 × His (N-His) were prepared (Supplementary Figure S1). The purified proteins were coated onto plates, and HisMab-1 binding was assessed by ELISA (Figure 1d). As expected, the apparent affinity of HisMab-1 increased with increasing His-tag length, probably due to an internal avidity effect, while binding to N-His was comparable to that observed for the C-terminal 6 × His construct (no significant difference in unpaired *t*-test). Of note, HisMab-1 binding was slightly restored in 4×His+AA compared with 4×His, suggesting that the peptide backbone following the 4 × His sequence assists in the interaction. This observation is consistent with our previous flow cytometry analysis, in which binding of HisMab-1 to CD20 carrying a 4 × His insertion in its extracellular loop was detectable [20]. Interestingly, among all the variants tested, HisMab-1 showed the strongest binding to 6×His+A. These results are discussed later.

Affinity measurement of HisMab-1 for polyhistidine peptides using ITC

Since kinetic analysis of HisMab-1 binding to the His-tag failed in SPR, we then used ITC to determine the equilibrium K_D values and thermodynamic parameters (ΔG, ΔH, and $-T\Delta S$). To obtain the binding parameters for the 1:1 interaction between HisMab-1 and the pentahistidine and hextahistidine peptides, we prepared a Fab fragment of HisMab-1 and used it for ITC. First, we analyzed the binding under pH 7.0 condition (Figure 2). The K_D values were determined to be 128 ± 19 nM for the pentahistidine peptide and 31 ± 8.4 nM for the hexahistidine peptide, indicating that HisMab-1 Fab exhibits approximately four-fold higher affinity for the longer peptide. As summarized in Figure 2b, the thermodynamic analysis revealed that the binding of the hexahistidine peptide was primarily enthalpy-driven with $\Delta G = -42$ kcal/mol, $\Delta H = -41 \pm 0.7$ kcal/mol, and $-T\Delta S = 2$ kcal/mol.

To obtain information on the pH dependence of the binding, analyses were also performed under pH 5.5, 6.0, 6.5, 7.5, and 8.5 (Table 1 and Supplementary Figure S2). The binding affinity of HisMab-1 Fab for the hexahistidine peptide was essentially unchanged between pH 6.0 and 8.5, with K_D values ranging from 24 to 31 nM. In contrast, the pentahistidine peptide showed reduced binding at pH 6.0 and 8.5 compared with that at neutral pH, suggesting that the shorter tag is more sensitive to environmental conditions. At pH 5.5, where the protonation state of histidine side chains changes, no appreciable binding was observed for either peptide, indicating that acidic conditions disrupt the interaction. Overall, these data demonstrate that HisMab-1 maintains stable binding to the hexahistidine peptide across the broad pH range typically used in standard biochemical experiments.

Evaluation of the specificity of HisMab-1 binding to a His-tagged protein

Next, to evaluate whether HisMab-1 is helpful for the specific detection of His-tagged proteins, we performed western blot analysis. The C-terminally hexahistidine-tagged Immunoglobulin-degrading Enzyme from *Streptococcus pyogenes* (IdeS-His) was expressed in *E. coli* under a suboptimal condition to suppress the expression level. The lysate was directly subjected to sodium dodecyl sulfate polyacrylamide gel electrophoresis (SDS-PAGE), confirming its expression at a moderate level (Figure 3a). After transferring the proteins to a membrane, they were probed with HisMab-1 at concentrations of 0.1, 0.3, 1, or 3 μg/ml. As shown in Figure 3b, HisMab-1 at 0.1 μg/ml clearly detected IdeS-His, and the signal intensity of the band was saturated at a concentration of 0.3 μg/ml. Even at 3 μg/ml, almost no bands other than IdeS-His were observed, suggesting the high specificity of HisMab-1 for His-tagged proteins. For a more detailed assessment of the specificity of HisMab-1, 0, 0.1, 1, and 10 ng of purified IdeS-His were added to crude lysates from bacterial (*E. coli*) and mammalian (CHO-K1) cells, and the samples were analyzed by western blotting using 0.3 μg/ml HisMab-1 (Figure 3c and Supplementary Figure S3). As a result, IdeS-His could be detected even at 0.1 ng, demonstrating the high sensitivity of HisMab-1. In the CHO-K1 lysate, weak additional bands were observed around 70–90 kDa; apart from these, only minimal nonspecific signals were detected in either lysate. These results indicate that HisMab-1 can be reliably used to detect target proteins from crude samples, such as bacterial and mammalian cell extracts, in most practical applications.

a

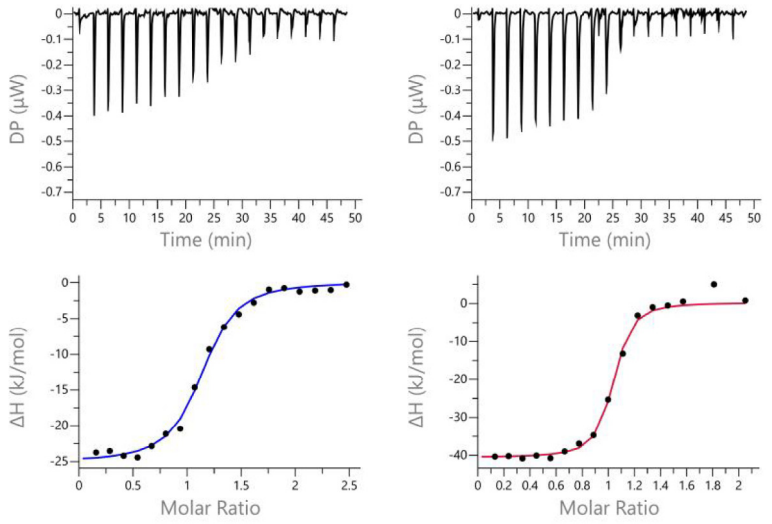

b

	Pentahistidine	Hexahistidine
K_D (nM)	128 ± 19	31 ± 8.4
ΔG (kcal/mol)	−39	−42
ΔH (kcal/mol)	−25 ± 0.5	−41 ± 0.7
$-T\Delta S$ (kcal/mol)	14	2
N	1.10 ± 0.01	0.99 ± 0.01

Figure 2. ITC analysis of the interaction between HisMab-1 Fab and polyhistidine peptides. (a) Raw heat trace (top) and integrated heat plot (bottom) fitted using a one-site binding model for the binding of HisMab-1 Fab to pentahistidine (left) and hexahistidine (right) peptides. Similar results were obtained in two independent experiments (n = 2), and representative data are shown. (b) Summary of the thermodynamic parameters.

Table 1 ITC-derived dissociation constants (K_D) and stoichiometries (N) for the binding of penta- and hexa-histidine peptides to HisMab-1 Fab at various pH values.[a]

Peptide	pH	Cell [μM]	Syringe [μM]	K_D [nM]	N
Pentahistidine	5.5	5.4	70	n.d.	–
	6.0	9.1	70	580 ± 82	1.03 ± 0.02
	6.5	7.2	70	170 ± 20	1.01 ± 0.01
	7.0	5.5	70	128 ± 19	1.10 ± 0.01
	7.5	6.9	50	290 ± 20	1.02 ± 0.01
	8.5	5.6	60	4300 ± 500	1.00 ± 0.05
Hexahistidine	5.5	5.4	70	n.d.	–
	6.0	5.4	70	24 ± 5.5	1.02 ± 0.01
	6.5	3.4	70	27 ± 4.1	0.94 ± 0.01
	7.0	6.6	70	31 ± 8.4	0.99 ± 0.01
	7.5	5.0	40	26 ± 3.7	0.94 ± 0.01
	8.5	3.7	40	28 ± 4.6	0.98 ± 0.01

[a] Measurements were performed using different buffer systems optimized for each pH range (acetate buffer at pH 5.5, MES buffer at pH 6.0–6.5, and potassium phosphate buffer at pH 7.0–8.5). Because the buffer ionization enthalpy differs among these systems, the apparent enthalpy changes (ΔH) cannot be directly compared across conditions and are therefore not shown. Only K_D and N values derived from one-site binding model fits are presented. Errors represent fitting uncertainties.

Crystallographic analysis of the HisMab-1 apo-form

To obtain structural information on HisMab-1, we first analyzed the structure of its apo-form Fab. Crystallization screening yielded crystals under 18 out of 864 conditions. After optimizing the crystallization conditions, we determined the apo-form structure at a resolution of 2.39 Å (Figure 4a,

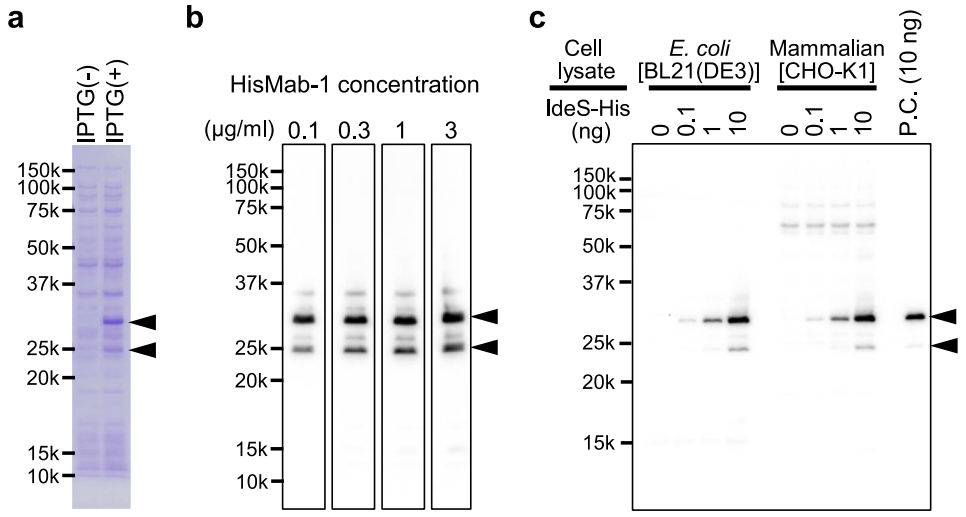

Figure 3. Western blotting analysis of His-tagged IdeS protease using HisMab-1. (a, b) Total cell lysates of *E. coli* BL21(DE3) before and after IPTG induction were subjected to 12.5% SDS–PAGE under reducing conditions. The proteins were stained with CBB (a) or transferred to a polyvinylidene difluoride (PVDF) membrane (b). The membrane was cut into lanes and incubated with varying concentrations of HisMab-1 for 1 h, followed by detection using an HRP-conjugated goat anti-mouse IgG antibody. Note that IdeS-His was expressed as two bands, and the lower band is thought to be derived from IdeS-His that was cleaved at the N-terminal flexible region during production. (c) Detection of IdeS-His from *E. coli* BL21(DE3) and CHO-K1 cell lysates. The indicated amounts of purified of IdeS-His was added to the cell lysates and analyzed by western blotting as in (b). 10 ng of purified IdeS-His alone (without lysate) was used as a positive control (P.C.). Arrowheads indicate the bands corresponding to IdeS-His.

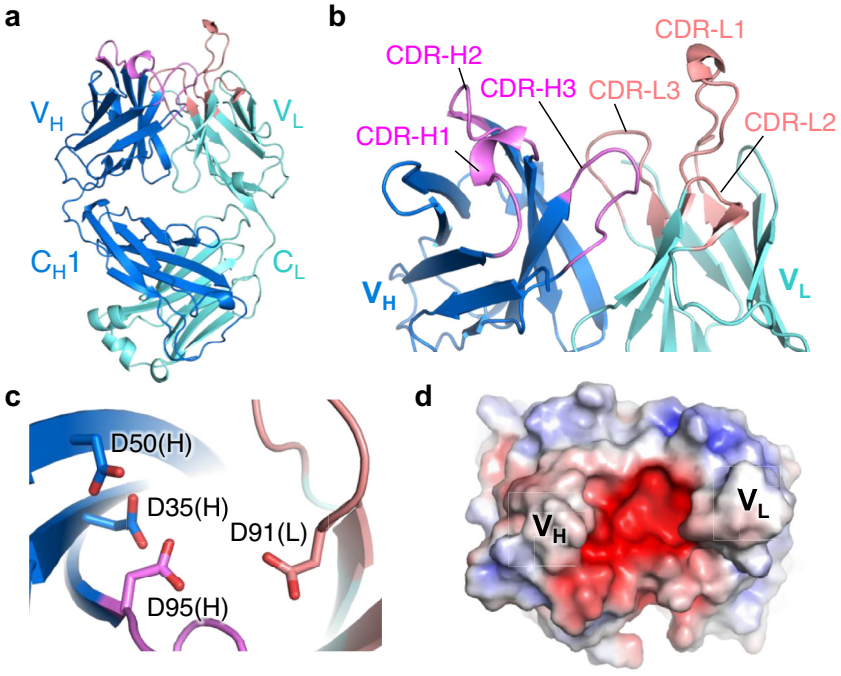

Figure 4. Crystal structure of HisMab-1 Fab in the apo form. (a, b) Cartoon representation of the overall structure (a) and the close-up view of the Fv region (b) of the HisMab-1 Fab. The heavy and light chains are shown in marine blue and cyan, respectively. The CDR loops of the heavy and light chains are highlighted in magenta and salmon, respectively. (c) Acidic antigen binding cleft formed by Asp35, Asp50, and Asp95 of the heavy chain, and Asp91 of the light chain. (d) Electrostatic surface potential of the antigen-binding cleft of HisMab-1, contour at ±5 kT/e. The calculation was performed using the APBS software [21].

Table 2 Data collection and refinement statistics.

	Apo form	Peptide-bound form
Data collection		
Beamline	PF BL-1A	SPring-8 BL44XU
Wavelength (Å)	1.052	0.900
Space group	$C222_1$	$P2_1$
Unit-cell parameters		
a, *b*, *c* (Å)	73.7, 191.0, 177.3	54.1, 69.5, 93.4
α, β, γ (°)	90.0 90.0 90.0	90.0, 93.8, 90.0
Resolution (Å)	48.2–2.39 (2.47–2.39)	48.13–2.39 (2.54–2.39)
R_{sym} (%)	10.1 (114.5)	6.3 (104.3)
$I/\sigma I$	17.1 (2.2)	11.0 (1.21)
CC1/2 (%)	99.9 (94.6)	99.8 (49.2)
Completeness (%)	99.9 (100.0)	99.0 (97.3)
Redundancy	13.9 (14.4)	3.5 (3.6)
Refinement		
Resolution (Å)	48.20–2.39	39.57–2.39
No. reflections	49,856	27,174
R_{work}/R_{free} (%)	23.15/28.84	19.56/23.70
No. atoms		
Protein	6607	5096
Peptide	–	122
Water/Ions	97	12
B-factors (Å^2)		
Protein	45.5	80.3
Peptide	–	69.0
Water/Ions	68.7	58.7
Ramachandran		
Favored (%)	95.9	96.2
Allowed (%)	4.1	3.6
R.m.s. deviations		
Bond lengths (Å)	0.009	0.006
Bond angles (°)	1.019	0.819

Values in parentheses are for highest resolution shell.

Table 2). The crystal contained two Fab molecules (mol-1 and mol-2) in the asymmetric unit. In the crystal, the antigen-binding site of each molecule is covered by the constant region of a neighboring molecule (Supplementary Figure S4a). This interaction may contribute to stabilizing the complementarity-determining region (CDR) loops even in the absence of antigen, allowing us to model all CDR loops in the crystal structure (Figure 4b).

The root mean square deviation (RMSD) for the superposition of the two molecules in the asymmetric unit was 0.595 Å for the overall structure (for 366 Cα atoms), and 0.322 Å for the Fv region (for 214 Cα atoms). No significant structural differences were observed between the two molecules in the Fv region, including CDR loops (Supplementary Figure S4b). At the center of the groove formed between V_H and V_L, there is a cluster of aspartic acid residues—Asp35, Asp50, and Asp95 of the heavy chain, and Asp91 of the light chain (Figure 4c)—forming an acidic antigen-binding cleft (Figure 4d). Such a negative surface potential at the antigen-binding site is a characteristic also seen in 3D5 and may be advantageous for attracting and/or accommodating the His-tag, which tends to be partially positively charged under physiological conditions [19].

Crystallographic analysis of HisMab-1 in complex with the hexahistidine peptide

As the antigen-binding site was covered by a neighboring molecule in the apo-form crystal packing, we performed a crystallization screening of HisMab-1 Fab again in the presence of a hexahistidine peptide to obtain complex crystals. However, screening under 576 conditions did not yield any crystals of the complex. Therefore, we converted HisMab-1 into Fv-clasp, a hyper-crystallizable antibody fragment format [22], and performed a screening in the presence of the peptide. Crystals appeared under 4 out of 192 conditions. After optimizing the conditions, we successfully determined the complex structure at a resolution of 2.39 Å (Figure 5a, Table 2). This crystal also contained two Fv-clasp molecules (mol-1 and mol-2) in the asymmetric unit. In both molecules, electron density corresponding to the

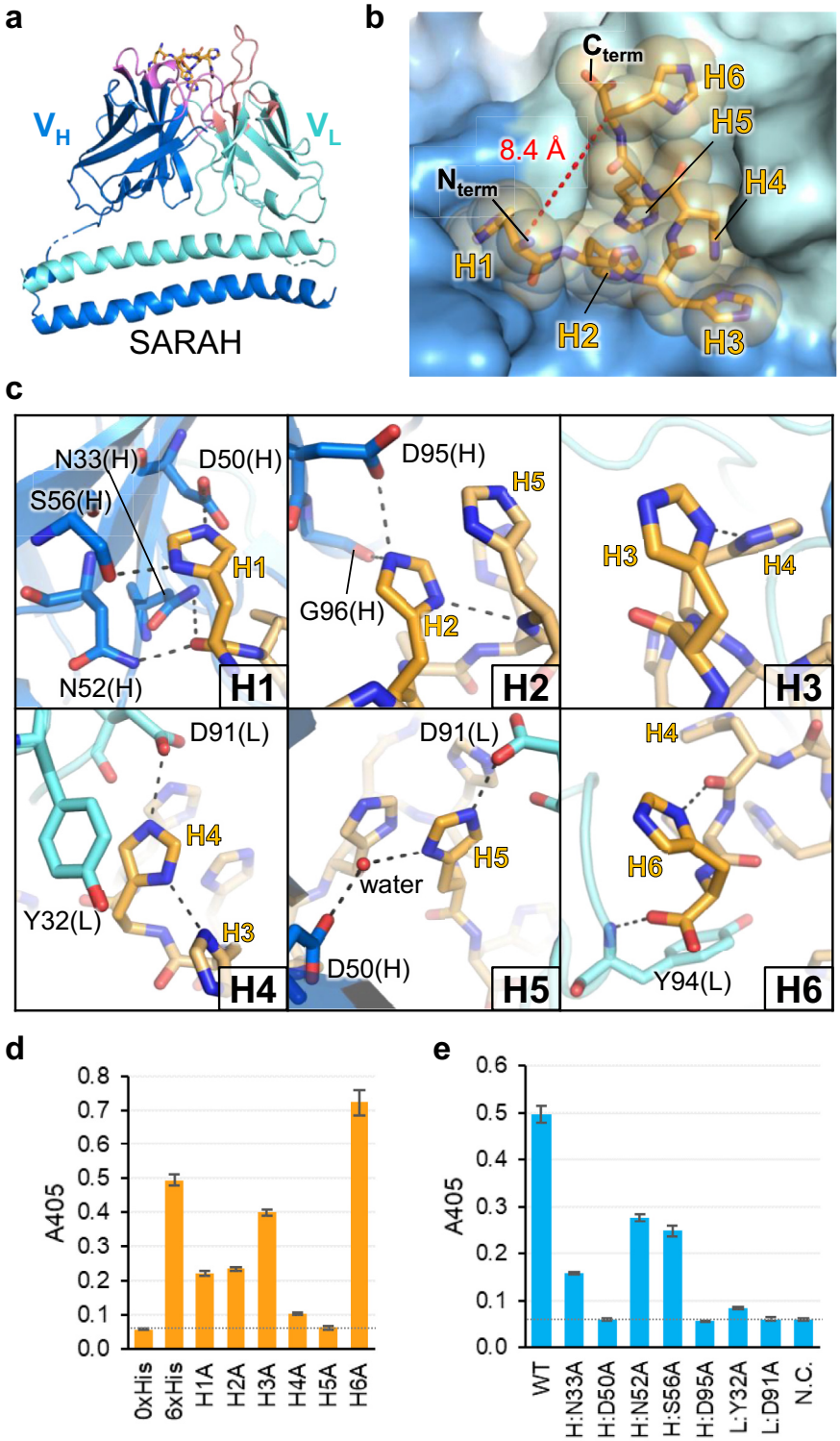
a
VH
VL
SARAH
b
Cterm
H6
H5
8.4 Å
Nterm
H4
H1
H2
H3
c
N33(H)
D50(H)
S56(H)
H1
N52(H)
H1
D95(H)
H5
G96(H)
H2
H2
H3
H4
H3
D91(L)
H4
Y32(L)
H3
H4
D91(L)
H5
water
D50(H)
H5
H4
H6
Y94(L)
H6
d
A405
0.8
0.7
0.6
0.5
0.4
0.3
0.2
0.1
0.0
0xHis
6xHis
H1A
H2A
H3A
H4A
H5A
H6A
e
A405
0.6
0.5
0.4
0.3
0.2
0.1
0.0
WT
H:N33A
H:D50A
H:N52A
H:S56A
H:D95A
L:Y32A
L:D91A
N.C.

hexahistidine peptide was observed at the antigen-binding site (Supplementary Figure S4c). The RMSD for the superposition of the two molecules in the asymmetric unit was 0.737 Å for the overall structure (for 285 Cα atoms), and 0.273 Å for the Fv region (for 201 Cα atoms, Supplementary Figure S4d). When each of the mol-1 molecules in the apo-form and the complex-form was superposed based on the Fv region, the RMSD was 0.329 Å for 202 Cα atoms, and surprisingly, even including the side chains, the RMSD value was only 0.382 Å for 1421 atoms (Supplementary Figure S4e). This strongly suggests that HisMab-1 undergoes little structural change upon peptide binding, consistent with the ITC result showing minimal entropy change upon binding ($-T\Delta S = 2$ kcal/-mol, Figure 2b).

All six histidine residues of the hexahistidine peptide could be assigned to the electron density at the antigen-binding site of HisMab-1, where the peptide adopts a compact folded configuration (Supplementary Figure S4c). The side chains of His1, His2, His4, and His5 of the peptide are oriented toward the groove, whereas the side chains of His3 and His6 lie on the surface of HisMab-1 (Figure 5b). All six histidine residues are in contact with HisMab-1, but to varying degrees. When the contact area between each histidine side chain and HisMab-1 was calculated using PISA [23], the areas of His3 and His6 were somewhat smaller than those of the other residues (Table 3). In addition, as shown in Figure 5c, the side chains of His1, His2, His4, and His5 each form one or two hydrogen bonds with the antibody, whereas those of His3 and His6 do not. The side chain of His4 also forms a stacking interaction with Tyr32 of the light chain. These observations suggest that HisMab-1 has six pockets to accommodate histidine residues, but the histidine residues in the third and sixth pockets contribute relatively little to binding. The limited contribution of the sixth histidine residue may explain why HisMab-1 can bind the pentahistidine peptide, albeit at moderate affinity (Figure 2b). In the crystal structure, several intra-peptide interactions were also observed. Hydrogen bonds are formed between the side chain of His2 and the main chain of His5, the side chains of His3 and His4, and the main chain of His4 and the side chain of His6. Additionally, the imidazole rings of His2 and His5 form a stacking interaction with each other (Figure 5c). These interactions may contribute to stabilizing the peptide in its compact configuration within the antigen-binding site.

Mutational analysis to evaluate the contribution of individual residues to binding

For evaluating the contribution of each histidine residue within the His-tag to HisMab-1 binding, we performed an alanine-scanning analysis in the context of ACE2-6×His (Supplementary Figure S1). The binding was evaluated by ELISA, as in Figure 1a (Figure 5d). H1A and H2A showed signals less than half of that observed with the parent 6×His. Furthermore, the signal of H4A was markedly reduced, and that of H5A was almost completely lost. These results indicate that His4 and His5 contribute most significantly to the interaction. In contrast, His3, which showed little interaction with HisMab-1 in the crystal structure, retained approximately 80% of the signal when substituted with alanine. Unexpectedly, H6A exhibited enhanced binding. This observation suggests that the side chain of the sixth histidine is slightly unfavorable for binding. Considering that the carboxyl group of the sixth histidine forms a hydrogen bond with HisMab-1 in the crystal structure (Figure 5c), that HisMab-1 shows lower affinity for 5×His (Figure 1b–d), and that HisMab-1 binding to H6A is comparable to that observed for 6×His+A (Figure 1c), it is likely that HisMab-1 achieves maximal affinity when its sixth pocket is occupied by a small amino acid such as alanine.

We also introduced alanine substitutions into HisMab-1 residues whose side chains were observed to interact with the hexahistidine peptide in the crystal structure (Figure 5c). The three mutants involving neutral amino acids (i.e., H:N33A, H:N52A, and H:S56A) had only partial impact on binding, whereas substitution of the

Figure 5. Crystal structure of HisMab-1 Fv-clasp in complex with the hexahistidine peptide. (a) Overall structure of the HisMab-1 Fv-clasp/hexahistidine peptide complex. HisMab-1 Fv-clasp is shown as a cartoon representation using the same color scheme as Figure 3a. The hexahistidine peptide is shown as an orange stick model. (b) The expanded view of the antigen binding site of HisMab-1. HisMab-1 is shown as a surface model, and the hexahistidine peptide is shown as a stick model with a transparent sphere model. (c) Interaction between HisMab-1 and the peptide. Each panel shows an enlarged view of the area surrounding each residue of the hexahistidine peptide. Dashed lines denote hydrogen bonding interactions. (d) Alanine scanning of the His-tag. Each histidine residue in ACE2-6×His was individually substituted with alanine, and HisMab-1 binding to those variants was analyzed by ELISA. A dotted line indicates the A_{405} value of the negative control (0×His). Data represent the mean ± SEM of three independent experiments. (e) Mutational analysis of HisMab-1. Asn33, Asp50, Asn52, Ser56, and Asp95 in the heavy chain, and Tyr32 and Asp91 in the light chain, were substituted with alanine, and the contribution of each side chain to His-tag recognition was evaluated by ELISA. A dotted line indicates the A_{405} value of the negative control (N.C.) in which PBS was used instead of HisMab-1. Data represent the mean ± SEM of three independent experiments.

Table 3 Contact area between the sidechain of each residue of the hexahistidine peptide and HisMab-1 calculated using PISA [23].

Residue	His1	His2	His3	His4	His5	His6
Contact area (Å^2)	111.7	105.9	91.7	127.4	129.3	83.8

three aspartic acid residues (i.e., H:D50A, H:D95A, and L:D91A) led to complete loss of binding (Figure 5e). Because these aspartic acid residues are involved in forming the acidic cleft shown in Figure 4d, they may contribute not only to the stabilization of the interaction after binding but also to the initial long-range attraction of the His-tag before complex formation. The binding of the L:Y32A mutant was also almost abolished, indicating a crucial role of the stacking interaction between Tyr32(L) and His4 in binding.

Loop insertion application of the HisMab-1/ hexahistidine-tag system

We have previously shown that HisMab-1 can bind to the His-tag inserted into the extracellular loop region of the membrane protein CD20 using flow cytometry analysis [20]. However, the loop in which the His-tag was inserted is over 40 residues long and is structurally flexible, allowing the inserted His-tag to assume a conformation compatible with HisMab-1 binding efficiently. Therefore, in the current study, we investigated whether HisMab-1 can bind to His-tag inserted into a more structurally restricted region, such as a β-hairpin. As a model protein, we chose MBP. MBP has a short antiparallel β-sheet protruding from its surface, with the two strands connected by only two residues (i.e., Asn173 and Gly174). We inserted six histidine residues between these two residues together with a few spacer residues (designated MBP-iHis; Figure 6a) and expressed it in *E. coli*. MBP-iHis was produced as a soluble protein and could be purified using the IMAC method, similar to its general terminal tag version (Supplementary Figure S5a). Moreover, this sample could also be purified using amylose resin, to which functional MBP specifically binds (Supplementary Figure S5b), suggesting that inserting the His-tag in the β-hairpin loop had negligible effect on the function or the folding of the target molecule.

We quantitatively measured the affinity between HisMab-1 Fab and MBP-iHis using ITC. The resulting K_D value was calculated to be 38 ± 8.3 n M (Figure 6b), indicating that HisMab-1 binds to the His-tag inserted into the β-hairpin loop with roughly the same affinity as it does to the free peptide (Figure 2). We also tested whether HisMab-1 Fab and MBP-iHis form a stable complex in solution using size-exclusion chromatography (SEC). As shown in Figure 6c, their mixture exhibited a monodisperse peak eluting earlier than the peaks of the individual proteins. SDS-PAGE analysis confirmed that this peak contained both proteins, demonstrating stable complex formation (Figure 6d).

Finally, we also performed preliminary cryo-electron microscopy (cryo-EM) analysis of the complex sample. From a total 1776 micrographs, 56,517 particles were extracted and subjected to 2D classification. The resulting class averages exhibited densities corresponding to MBP and the Fab, and several classes showed features consistent with the predicted complex model (Supplementary Figure S5c). Although the target molecule is not particularly large (MBP: 42 kDa) for single-particle analysis (SPA), binding of the HisMab-1 Fab (48 kDa) to the loop-inserted His-tag increased the apparent molecular size, thereby facilitating visualization.

Discussion

In this study, we investigated the binding properties of HisMab-1 to His-tags from multiple perspectives. From the binding analyses, we found that at least five histidine residues are required for HisMab-1 to exhibit clear binding to the His-tag. The crystal structure revealed that HisMab-1 possesses six histidine-binding pockets in its antigen-binding site, but the side chain of the histidine residue occupying the sixth pocket does not appear to contribute to the interaction. The alanine-scanning results further showed that the side chain at this position is rather unfavorable for the interaction. Thus, the optimal tag sequence for HisMab-1 appears to be “HHHHHA”. Nevertheless, the results of the pull-down assay (Figure 1c) and western blotting (Figure 3) demonstrated that a 6-residue His-tag performs sufficiently well for the practical use of HisMab-1. In addition, HisMab-1 binding to the N-terminal 6 × His (note that a bulky glutamine residue follows the N-terminal 6 × His in our construct, Supplementary Figure S1a) was comparable to that observed for the C-terminal 6 × His (Figure 1d), indicating that HisMab-1 can recognize the 6 × His-tag equally well regardless of whether it is attached to the N- or C-terminus of the target protein. The 6-residue His-tag is the most commonly used length among His-tags, as it provides sufficiently high affinity for Ni^{2+}-immobilized resin in IMAC [24], and vectors for fusing a 6-residue His-tag to target proteins are commercially available for a wide range of expression systems. Therefore, HisMab-1 is an antibody that many researchers will find convenient to use.

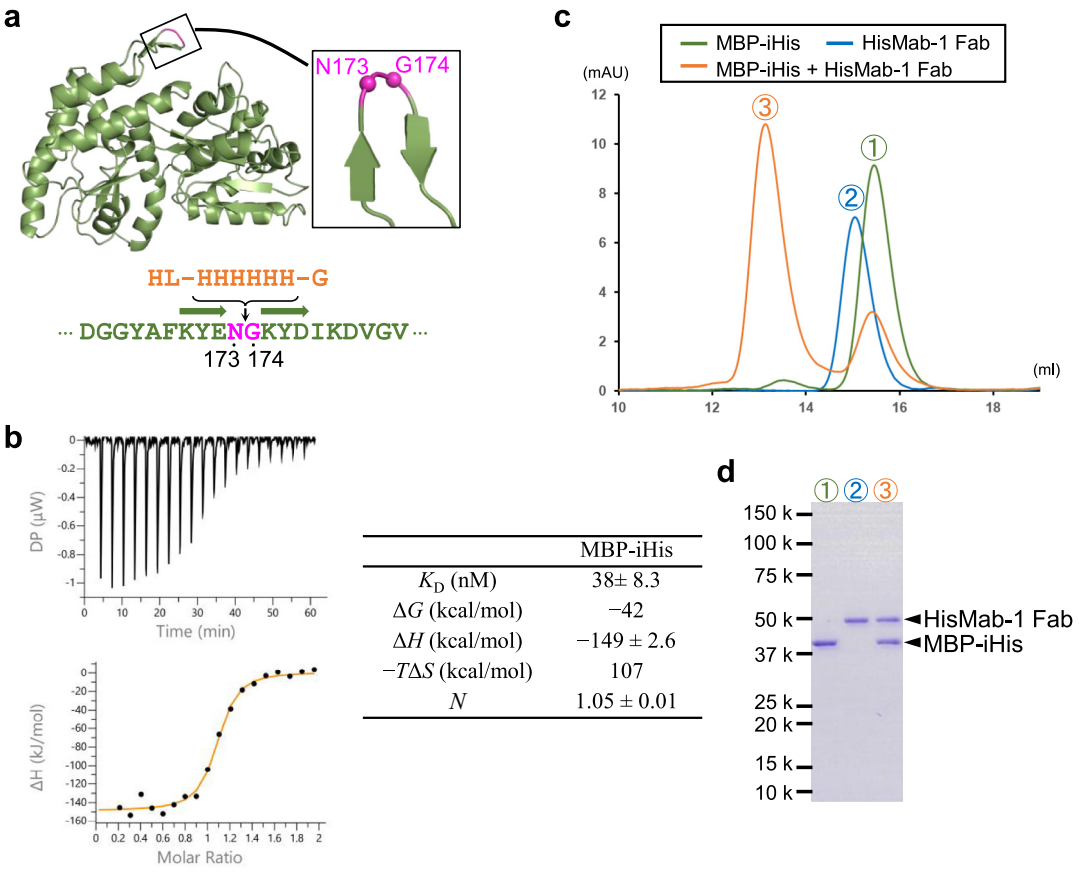

Figure 6. Binding of HisMab-1 to the His-tag inserted into the β-hairpin loop of MBP. (a) The overall structure of MBP (PDB: 1ANF) is depicted as a cartoon model, with an enlarged view of the β-hairpin loop where the hexahistidine sequence was inserted. The inserted sequence comprises a hexahistidine tag flanked by HL at the N-terminus and G at the C-terminus (HL-HHHHHH-G), designed to provide flexibility and minimize structural perturbation. The amino acid sequence surrounding the β-hairpin loop is provided below. (b) ITC analysis of HisMab-1 Fab interaction with MBP-iHis protein. Thermograms and fitted thermodynamic parameters for the binding of HisMab-1 Fab to MBP-iHis. Data were fitted using a single-site binding model to derive K_D, ΔG, ΔH, $-T\Delta S$, and binding stoichiometry (N). The fitted stoichiometry ($N = 1.05 \pm 0.01$) is consistent with a 1:1 binding mode within experimental error. Similar results were obtained in two independent experiments ($n = 2$), and representative data are shown. (c, d) Size-exclusion chromatography (SEC) analysis to assess complex formation between MBP-iHis and HisMab-1 Fab. MBP-iHis, HisMab-1 Fab, and their mixture were subjected to SEC analysis on a Superdex 200 Increase 10/300 column (c). 5–20% gradient SDS-PAGE was then used to analyze the peak fraction samples under non-reducing conditions (d).

We also demonstrated that HisMab-1 possesses a unique feature that distinguishes it from other anti-His-tag antibodies: it can bind to a His-tag inserted into the tight hairpin loop of the protein. Not only anti-His-tag antibodies but also most anti-epitope tag antibodies typically cannot bind to, or show significantly reduced affinity for, tag peptides inserted into structurally highly constrained loop regions of proteins. This is because, when these tags bind to antibodies, they usually adopt an extended conformation with both terminal ends pointing in opposite directions [25–28]. However, in our previous study, we found through crystallographic analysis that two epitope tags, namely the PA-tag and MAP-tag, adopt a U-shaped conformation with both terminal ends exposed to the solvent when bound to their respective antibodies (NZ-1 and PMab-1, respectively), which led to the discovery of their compatibility with loop insertion [13,29]. This structural feature, observed in the PA-tag/NZ-1 and MAP-tag/PMab-1 complexes, is essential for antibodies to recognize tags inserted into loops with the same efficiency as those fused to termini. Notably, the conformation of the hexahistidine peptide bound to HisMab-1 is in perfect agreement with this requirement (Figure 5), warranting its compatibility with the loop-insertion applications.

One significant advantages of loop region tag insertion is its applicability to proteins for which terminal tagging is structurally or functionally impractical. Protein termini are sometimes intracellular, essential for function, or structurally

buried, making terminal tag addition unfeasible or disruptive. In such cases, internal tags offer a practical alternative that can avoid these issues. Moreover, internal tags can function as "mobile epitopes" enabling site-specific antibody binding. This application is particularly advantageous for structural analysis using cryo-EM. In cryo-EM SPA, antibody fragments are often attached to target molecules to stabilize their structure, increase their apparent molecular weight, or serve as fiducial markers. Normally, a mAb that recognizes the native three-dimensional structure of the target protein must be developed individually for this purpose, because antibody fragments bound to terminal tags are generally unsuitable due to the high flexibility of the tag region relative to the target molecule. However, tags inserted into structurally constrained loop regions have low flexibility and behave more like intrinsic epitopes. Therefore, the loop-insertion-compatible tag system is expected to offer advantages in SPA, similarly to the protein-specific mAbs. In fact, Ji et al. recently succeeded in determining the cryo-EM structure of the human norepinephrine transporter by strategically employing an inserted PA-tag and the NZ-1 Fv-clasp [30]. In this study, we also obtained preliminary cryo-EM images of the MBP-iHis/HisMab-1 Fab complex, in which MBP and the Fab were clearly distinguishable in the 2D class averages (Supplementary Figure S5c). Although further optimization of the inserted sequence and its position, to reduce the flexibility between the target molecule and Fab, will be required to achieve higher-resolution reconstructions, our results suggest that the His-tag/HisMab-1 pair could serve as a promising tool for cryo-EM SPA, similar to the PA-tag/NZ-1 system.

Our comprehensive analyses establish HisMab-1 as one of the most dependable anti-His-tag antibodies, underpinned by robust structural and functional data. Furthermore, as demonstrated here, HisMab-1 is a highly versatile antibody that is compatible with most commonly used His-tag lengths, regardless of their placement position in the target protein. Given the widespread use of the His-tag in cost-effective protein purification via IMAC, HisMab-1 serves as an ideal reagent for diverse applications in life science research. Altogether, HisMab-1 provides a valuable platform for future methodological developments in protein science and structural biology.

Materials and Methods

Sample preparation of His-tagged proteins

The PA-tag and His-tags of various designs were fused to the extracellular domain of human ACE2 (residues 18–615), and the resulting DNA fragments were subcloned into the pcDNA3.1 vector containing a mouse IgG kappa signal sequence. Individual plasmids were transfected into Expi293F cells (Thermo Fisher Scientific) cultured according to the manufacturer's protocol. For SPR and ELISA analyses, the proteins were purified from the culture supernatant using NZ-1-immobilized Sepharose, following a previously described protocol [16].

For the western blot analysis, a hexahistidine tag was appended to the C-terminus of IdeS protease (IdeS-His). The corresponding DNA segment was subcloned into the pET11c vector (Novagen), and the plasmid was transformed into the *E. coli* strain BL21(DE3) (Novagen). The transformed cells were cultured in LB medium at 37 °C in the presence of 50 mg/ml ampicillin. When the optical density at 600 nm (A_{600}) reached 0.6, isopropyl-β-D-thiogalactopyranoside (IPTG) was added to a final concentration of 0.05 mM, and the culture was further incubated at 37 °C for 1 h. After cell lysis by sonication, IdeS-His was purified using Ni-NTA Agarose (Qiagen) and dialyzed against 20 mM Tris–HCl buffer (pH 8.0) containing 150 mM NaCl. *E. coli* cells lysed in SDS-PAGE sample buffer containing dithiothreitol and TurboNuclease (Accelagen) were also used for western blot analysis.

Sample preparation of MBP-iHis

The gene encoding the maltose-binding protein (MBP; UniProt ID: P0AEX9) was inserted into the pET-24b(+) vector (Novagen) to generate pET-24b(+)-MBP. To construct the loop-insertion variant, a hexahistidine tag flanked by linker residues (HL and G; HLHHHHHHG) was inserted between residues 173 and 174 of the MBP coding sequence, resulting in pET24b(+)-MBP-iHis. This insertion was introduced by site-directed mutagenesis using the following primers: forward, 5′-CATCATCATGGTGGTAAGTACGATATTAAA GACGTTGGC-3′ and reverse, 5′-ATGATGATG TAGGTGATTTTCGTATTTGAAAGCGTATCC-3′. The plasmid was then transformed into *E. coli* BL21 (DE3) cells. The cells were cultured in LB medium containing 50 μg/ml kanamycin at 37 °C. When A_{600} reached 0.5, IPTG was added to 0.1 mM, and the culture was incubated overnight at 18 °C.

Cell lysates were purified using Ni-NTA affinity chromatography (Qiagen). Cells were disrupted by sonication in lysis buffer (25 mM Tris–HCl, pH 8.0, 300 mM NaCl, 20 mM imidazole). After centrifugation (15,000*g*, 30 min, 4 °C), the supernatant was applied to a Ni-NTA resin pre-equilibrated with the same buffer. The resin was washed with wash buffer (25 mM Tris–HCl, pH 8.0, 300 mM NaCl, and 20 mM imidazole), and proteins were eluted with a buffer containing 500 mM imidazole.

The lysates were subjected to amylose affinity chromatography (New England Biolabs). Cells were lysed in MBP lysis buffer (20 mM Tris–HCl, pH 8.0, 300 mM NaCl), and the resulting

supernatant was applied to an amylose resin pre-equilibrated with the same buffer. After washing, MBP-tagged proteins were eluted with lysis buffer supplemented with 20 mM maltose.

Sample preparation of antibody fragments

For recombinant expression of HisMab-1 Fab, the DNA sequence encoding the signal peptide through the C_{H1} domain of the heavy chain and the full-length light chain was subcloned into the pCAG-Neo and pCAG-Ble expression vectors (FUJIFILM Wako Pure Chemical Corporation), respectively. These constructs were co-expressed in ExpiCHO-S cells, and the protein was purified using Capto L (Cytiva), followed by Protein G Sepharose 4 Fast Flow (Cytiva). For epitope-specific affinity purification, HisMab-1 Fab was further purified using a custom affinity column prepared by coupling a synthetic hexahistidine peptide to CNBr-activated Sepharose 4 B (Cytiva). After sample application and extensive washing with phosphate-buffered saline (PBS; 10 mM sodium phosphate buffer, pH 7.5, 150 mM NaCl), the bound HisMab-1 Fab was eluted with 0.1 M glycine-HCl buffer (pH 2.7), and the eluted fractions were immediately neutralized with 1 M Tris–HCl (pH 8.0). The purified fractions were subsequently dialysed against PBS to remove residual buffer components.

To prepare the HisMab-1 Fv-clasp, DNA encoding the V_L domain was fused to the SARAH domain derived from human MST1 containing an S37C mutation, while the V_H domain carrying an S112C mutation was fused to the SARAH domain without the mutation. The V_H(S112C)-SARAH segment was further fused to the human IgG1 Fc coding sequence. These DNA constructs were subcloned into the pcDNA3.1 vector (Thermo Fisher Scientific) and co-expressed in Expi293F cells. The Fv-clasp-Fc was purified with rProtein A Sepharose (Cytiva) and subsequently treated with IdeS protease to cleave between the Fv-clasp and Fc regions. The sample was further purified by size-exclusion chromatography (SEC) on a Superdex 200 Increase 10/300 GL column (Cytiva), followed by anion-exchange chromatography on a Mono Q 5/50 GL column (Cytiva) equilibrated with 50 mM Tris–HCl (pH 7.5).

SPR

For SPR analysis, the constant region of full-length HisMab-1 IgG was replaced with that of the human IgG1 (hcHisMab-1), and the resulting chimeric antibody was expressed in Expi293F cells and purified using rProtein A Sepharose. SPR analyses were conducted using a Biacore T200 instrument (Cytiva) with a flow rate of 30 μ l/min at 25 °C in a running buffer (137 mM NaCl, 10 mM Na_2HPO_4, 2.7 mM KCl, 1.8 mM KH_2PO_4 (PBS) containing 0.05% Tween20). The chimeric HisMab-1 IgG and human IgG1 Fc (control) were captured on the measurement and reference cells, respectively, of a CM5 sensor chip (Cytiva) via anti-human IgG (Fc) antibodies that were chemically immobilized on the chip using the Human Antibody Capture Kit (Cytiva). ACE2 samples with various tags, prepared in a two-fold serial dilution from 2048 nM to 1 nM, were flowed over the sensor chip to obtain sensorgrams.

ITC

ITC experiments were performed at 25 °C using either a MicroCal PEAQ-ITC or a MicroCal iTC200 instrument (Malvern Panalytical). All protein and peptide solutions were thoroughly degassed before measurements. To analyze the interaction between HisMab-1 Fab and histidine peptides, HisMab-1 Fab (typically 5–9 μM) in buffer containing 150 mM NaCl was titrated with either pentahistidine or hexahistidine peptide (40–70 μM) prepared in the same buffer. The buffer composition was adjusted according to the target pH: 50 mM Sodium acetate (pH 5.5), 50 mM MES (pH 6.0–6.5), 50 mM Potassium phosphate (pH 7.0–8.5). Each titration consisted of an initial 0.4 μl injection followed by 19 successive injections of 2.0–2.5 μl, with 150 s intervals between injections.

To examine the interaction between HisMab-1 Fab and MBP-iHis, ITC measurements were conducted using the MicroCal iTC200 instrument at pH 7.0. The sample cell contained 5.2 μM HisMab-1 Fab in 50 mM sodium phosphate buffer (pH 7.0) with 150 mM NaCl, and the syringe was loaded with 50 μM MBP-iHis. The injection scheme was identical to that described above.

Thermograms were baseline-corrected and integrated using the PEAQ-ITC Analysis Software (Malvern Panalytical). Thermodynamic parameters (K_D, ΔH, and ΔS) were obtained by fitting to a one-site binding model [31]. Detailed experimental conditions and thermodynamic parameters for each pH and titration setup are summarized in Table 1.

Pull-down assay

Conditioned media containing ACE2ec with various tags were incubated with NZ-1 or HisMab-1 immobilized Sepharose at room temperature for 2 h. The beads were washed three times with 20 mM Tris–HCl (pH 7.5), 150 mM NaCl, and bound proteins were eluted with SDS-PAGE sample buffer and analyzed by 12.5% SDS-PAGE under non-reducing conditions, followed by staining with Coomassie Brilliant Blue (CBB).

ELISA

96-Well immune plates (Thermo Fisher Scientific) were coated at room temperature for 3 h with His-tagged ACE2-PA (10 μg/ml ACE2), followed by an overnight blocking with 20% Blocking One (Nacalai Tesque, Inc.). Subsequently, 10 nM

hcHisMab-1 in PBS with 5% Blocking One was added to each well and incubated for 2 h at room temperature. The wells were then washed four times with PBS. To detect the bound antibody, HRP-conjugated goat anti-human secondary antibody (MP Biomedicals), diluted to 1:10,000 in PBS with 5% Blocking One, was added and incubated for 1 h at room temperature. The wells were washed four times with PBS. Color development was achieved by adding 100 μL of ABTS substrate solution (SeraCare), and the absorbance at 405 nm was measured using the Varioskan ALF Multimode Microplate Reader (Thermo Fisher Scientific).

Western blot analysis

The lysate of *E. coli* expressing IdeS-His was subjected to 12.5% SDS-PAGE under reducing conditions and transferred to a polyvinylidene difluoride (PVDF) membrane, followed by blocking with Blocking One (Nacalai Tesque, Inc.) for 1 h. The membranes were then incubated for 1 h with varying concentrations of HisMab-1 (0.1, 0.3, 1, or 3 μg/ml) diluted in 10 mM Tris–HCl (pH 8.0), 150 mM NaCl, and 0.05% Tween-20 (TBS-T) containing 5% Blocking One, followed by a 1-h incubation with HRP-conjugated goat anti-mouse IgG antibody (Sigma–Aldrich) diluted 1:4000 in TBS-T containing 5% Blocking One. The membranes were washed four or five times with TBS-T between each step. Detection was performed using the ECL Prime reagent (Cytiva), and signals were analyzed with an iBright Imaging System (Thermo Fisher Scientific).

For the titration experiment, cell lysates were prepared as follows: *E. coli* BL21(DE3) cells cultured in LB medium until the A_{600} reached 0.6 were lysed in SDS-PAGE sample buffer containing dithiothreitol and TurboNuclease. CHO-K1 cells cultured in RPMI-1640 medium (FUJIFILM Wako Pure Chemical Corporation) supplemented with 10% FCS were harvested, washed five times with PBS, and lysed in 50 mM HEPES (pH 7.6), 150 mM NaCl, 0.5% NP-40, 1 mM PMSF, 1 μM pepstatin A, and 10 μM leupeptin. Purified IdeS-His was added to each lysate to give final amounts of 0, 0.1, 1, and 10 ng per lane, and the resulting lysates from *E. coli* and CHO-K1 cells, corresponding to 10 μl of culture and 2.5×10^4 cells per lane, respectively, were subjected to 12.5% SDS-PAGE under reducing conditions. Western blotting was performed using the same protocol as described above with 0.3 μg/ml HisMab-1. After the western blot analysis, the membrane was stained with CBB.

Crystallization

The purified HisMab-1 Fab was concentrated to 9.7 mg/ml by ultrafiltration using Amicon Ultra (Merck Millipore). Crystallization screening was performed at 20 °C by the sitting-drop vapor diffusion method using a PXS crystallization robot [32]. Crystal Screen, Crystal Screen 2, PEG/Ion Screen, PEG/Ion Screen 2, Crystal Screen Cryo, Crystal Screen 2 Cryo, MembFac, and Index (all from Hampton Research); Wizard Classic 1 and 2 (Rigaku); Stura FootPrint and MIDASPlus (Molecular Dimensions); and The PEGs II Suite and Protein Complex Suite (QIAGEN) were used as reservoir solutions. After optimizing the crystallization conditions using the hanging-drop vapor diffusion method, diffraction-quality crystals were obtained in a solution containing 2.0 M ammonium sulfate, 0.1 M Tris–HCl (pH 7.0), and 0.1 M lithium sulfate.

To obtain complex crystals, HisMab-1 Fv-clasp was concentrated using Amicon Ultra and mixed with a hexahistidine peptide (FUJIFILM Wako Pure Chemical Corporation) to a final concentration of 3.7 mg/ml for HisMab-1 Fv-clasp and 1.85 mM for the peptide. Initial crystallization screening was performed at 20 °C by the sitting-drop vapor diffusion method using Wizard Classic 1 and 2 (Rigaku) and JCSG-plus (Molecular Dimensions). Based on the initial hits, crystallization conditions were optimized using the hanging-drop vapor diffusion method, and diffraction-quality crystals were obtained in a solution containing 16% (w/v) polyethylene glycol 3350, 0.1 M HEPES (pH 7.0), and 0.2 M $MgCl_2$.

Data collection, structure determination, and refinement

Before X-ray diffraction experiments, apo crystals were soaked in the reservoir solution supplemented with 20% (v/v) glycerol, while complex crystals were soaked in a cryoprotectant solution containing 35% (w/v) polyethylene glycol 3350, 0.1 M HEPES (pH 7.0), and 0.2 M $MgCl_2$. All crystals were flash-cooled in liquid nitrogen.

X-ray diffraction experiments of the apo and complex crystals were performed at beamlines BL-1A of Photon Factory (Tsukuba, Japan) and BL44XU of SPring-8 (Hyogo, Japan), respectively. Diffraction data were processed using the X-ray Detector Software [33]. Phases were determined by molecular replacement using PHASER [34], with PDB entries 1GHF (for Fab), 4M43, 2IMM, and 7CEA (for Fv-clasp) used as search models. The structures were refined with PHENIX [35], manually modified with COOT [36], and validated with MolProbity [37]. Data collection statistics and refinement parameters are summarized in Table 1. Structural figures were prepared with the PyMOL Molecular Graphics System (v.2.3.4).

SEC analysis

Complex formation between HisMab-1 Fab and MBP-iHis was confirmed by SEC analysis. HisMab-1 Fab and MBP-iHis were mixed at a 1:1.5 molar ratio. The mixture and each protein

sample were individually subjected to SEC using a Superdex 200 Increase 10/300 GL column, equilibrated with PBS.

Cryo-EM analysis

Purified MBP–iHis/HisMab-1 Fab complex at a concentration of 2.5 μM was applied (3 μL per grid) onto glow-discharged Quantifoil R1.2/1.3 Cu 300-mesh grids (Quantifoil Micro Tools GmbH). The grids were blotted for 3 s with a blot force of 5 at 4 °C and 100% humidity and vitrified in liquid ethane using a Vitrobot Mark IV (Thermo Fisher Scientific).

Cryo-EM data were collected on a CRYO ARM 300 II microscope (JEOL Ltd.) operated at 300 kV, equipped with an in-column energy filter (slit width 30 eV) and a Gatan K3 direct electron detector. Movies were recorded at a nominal magnification of 60,000×, corresponding to a calibrated pixel size of 0.77 Å/pixel, with a total electron dose of 50 $e^-/Å^2$ fractionated over 50 frames. A total of 1776 movies were acquired using SerialEM 3.8 [38] under a nominal defocus range of −1.0 to −2.0 μm.

All movie stacks were motion-corrected and dose-weighted using MotionCor2 [39], and contrast transfer function (CTF) parameters were estimated using CTFFIND4 [40]. A total of 56,517 particles were automatically picked and subjected to reference-free 2D classification using RELION 4.0 [41]. Class averages exhibiting clear secondary-structural features were selected for further analysis. For visualization, representative 2D class averages were displayed using RELION 4.0 [41]. No 3D reconstruction was performed at this stage due to the preliminary nature of the dataset.

A predicted structural model of the MBP–iHis/HisMab-1 Fab complex was generated using AlphaFold3 [42] based on an MBP construct containing an inserted hexahistidine peptide sequence and in combination with the HisMab-1 Fv-clasp and HisMab-1 Fab structures. Molecular graphics and figure preparation were performed using UCSF ChimeraX [43].

Accession numbers

The coordinates and structure factors of the crystal structures of the HisMab-1 Fab (apo form) and HisMab-1 Fv-clasp/hexahistidine peptide complex have been deposited at the protein data bank under accession codes PDB IDs: 9VX2 and 9VX3, respectively.

CRediT authorship contribution statement

Natsuki Hitomi: Investigation. **Satowa Hoshi:** Investigation. **Mika K. Kaneko:** Investigation. **Ryuichi Kato:** Resources. **Kenji Iwasaki:** Resources, Funding acquisition. **Junichi Takagi:** Resources, Funding acquisition. **Yukinari Kato:** Resources, Funding acquisition. **Ayaka Harada-Hikita:** Writing – review & editing, Supervision, Project administration, Investigation, Data curation, Visualization. **Takao Arimori:** Writing – review & editing, Writing – original draft, Visualization, Supervision, Project administration, Investigation, Funding acquisition, Data curation.

Funding

This work was supported in part by Japan Society for the Promotion of Science (JSPS) KAKENHI under grant numbers JP21H02416 and JP25K02215 to T.A.; by the Japan Agency for Medical Research and Development (AMED) under grant number JP25am0521010 (to Y.K. and T.A.); by the Research Support Project for Life Science and Drug Discovery [Basis for Supporting Innovative Drug Discovery and Life Science Research (BINDS)] from AMED under grant numbers JP19am0101083 to R.K., JP25ama121001 to K.I., JP25ama121011 to J.T. and JP25ama121008 to Y.K.

DATA AVAILABILITY

Data will be made available on request.

DECLARATION OF COMPETING INTEREST

The authors declare that they have no known competing financial interests or personal relationships that could have appeared to influence the work reported in this paper.

Acknowledgments

We would like to thank the staff of the beamlines at the Photon Factory and SPring-8 for their help with X-ray data collection. We are also grateful to the Structural Biology Research Center (SBRC) at KEK for providing access to the ITC instrument used in this study.

Appendix A. Supplementary material

Supplementary material to this article can be found online at https://doi.org/10.1016/j.jmb.2025.169574.

Received 27 July 2025;
Accepted 29 November 2025;
Available online 3 December 2025

Keywords:
polyhistidine tag;
antibody;

X-ray crystallography; surface plasmon resonance; isothermal titration calorimetry

† Contributed equally.

References

[1]. Nygren, P.A., Stahl, S., Uhlen, M., (1994). Engineering proteins to facilitate bioprocessing. *Trends Biotechnol.* **12**, 184–188. https://doi.org/10.1016/0167-7799(94)90080-9.

[2]. Smith, D.B., Johnson, K.S., (1988). Single-step purification of polypeptides expressed in *Escherichia coli* as fusions with glutathione s-transferase. *Gene* **67**, 31–40. https://doi.org/10.1016/0378-1119(88)90005-4.

[3]. Harper, S., Speicher, D.W., (2011). Purification of proteins fused to glutathione S-transferase. *Methods Mol. Biol.* **681**, 259–280. https://doi.org/10.1007/978-1-60761-913-0_14.

[4]. Maina, C.V., Riggs, P.D., Grandea 3rd, A.G., Slatko, B.E., Moran, L.S., Tagliamonte, J.A., et al., (1988). An *Escherichia coli* vector to express and purify foreign proteins by fusion to and separation from maltose-binding protein. *Gene* **74**, 365–373. https://doi.org/10.1016/0378-1119(88)90170-9.

[5]. di Guan, C., Li, P., Riggs, P.D., Inouye, H., (1988). Vectors that facilitate the expression and purification of foreign peptides in *Escherichia coli* by fusion to maltose-binding protein. *Gene* **67**, 21–30. https://doi.org/10.1016/0378-1119(88)90004-2.

[6]. Esposito, D., Chatterjee, D.K., (2006). Enhancement of soluble protein expression through the use of fusion tags. *Curr. Opin. Biotechnol.* **17**, 353–358. https://doi.org/10.1016/j.copbio.2006.06.003.

[7]. Kapust, R.B., Waugh, D.S., (1999). *Escherichia coli* maltose-binding protein is uncommonly effective at promoting the solubility of polypeptides to which it is fused. *Protein Sci.* **8**, 1668–1674. https://doi.org/10.1110/ps.8.8.1668.

[8]. Kataeva, I., Chang, J., Xu, H., Luan, C.H., Zhou, J., Uversky, V.N., et al., (2005). Improving solubility of *Shewanella oneidensis* MR-1 and *Clostridium thermocellum* JW-20 proteins expressed into *Escherichia coli*. *J. Proteome Res.* **4**, 1942–1951. https://doi.org/10.1021/pr050108j.

[9]. Raran-Kurussi, S., Waugh, D.S., (2012). The ability to enhance the solubility of its fusion partners is an intrinsic property of maltose-binding protein but their folding is either spontaneous or chaperone-mediated. *PLoS One* **7**, e49589. https://doi.org/10.1371/journal.pone.0049589.

[10]. Raran-Kurussi, S., Keefe, K., Waugh, D.S., (2015). Positional effects of fusion partners on the yield and solubility of MBP fusion proteins. *Protein Expr. Purif.* **110**, 159–164. https://doi.org/10.1016/j.pep.2015.03.004.

[11]. Hopp, T.P., Prickett, K.S., Price, V.L., Libby, R.T., March, C.J., Cerretti, D.P., et al., (1988). A short polypeptide marker sequence useful for recombinant protein identification and purification. *Nature Biotechnol.* **6**, 1204–1210. https://doi.org/10.1038/nbt1088-1204.

[12]. Fujii, Y., Kaneko, M.K., Kato, Y., (2016). MAP Tag: a novel tagging system for protein purification and detection. *Monoclon. Antib. Immunodiagn. Immunother.* **35**, 293–299. https://doi.org/10.1089/mab.2016.0039.

[13]. Wakasa, A., Kaneko, M.K., Kato, Y., Takagi, J., Arimori, T., (2020). Site-specific epitope insertion into recombinant proteins using the map tag system. *J. Biochem.*. https://doi.org/10.1093/jb/mvaa054.

[14]. Field, J., Nikawa, J., Broek, D., MacDonald, B., Rodgers, L., Wilson, I.A., et al., (1988). Purification of a RAS-responsive adenylyl cyclase complex from *Saccharomyces cerevisiae* by use of an epitope addition method. *Mol. Cell Biol.* **8**, 2159–2165. https://doi.org/10.1128/mcb.8.5.2159-2165.1988.

[15]. Evan, G.I., Lewis, G.K., Ramsay, G.B., Bishop, J.M., (1985). Isolation of monoclonal antibodies specific for human c-myc proto-oncogene product. *Mol. Cell Biol.* **5**, 3610–3616. https://doi.org/10.1128/mcb.5.12.3610-3616.1985.

[16]. Fujii, Y., Kaneko, M., Neyazaki, M., Nogi, T., Kato, Y., Takagi, J., (2014). PA tag: a versatile protein tagging system using a super high affinity antibody against a dodecapeptide derived from human podoplanin. *Protein Express. Purif.* **95**, 240–247. https://doi.org/10.1016/j.pep.2014.01.009.

[17]. Hochuli, E., Bannwarth, W., Döbeli, H., Gentz, R.S., (1988). Genetic approach to facilitate purification of recombinant proteins with a novel metal chelate adsorbent. *Nature Biotechnol.* **6**, 1321–1325. https://doi.org/10.1038/nbt1188-1321.

[18]. Bornhorst, J.A., Falke, J.J., (2000). Purification of proteins using polyhistidine affinity tags. *Methods Enzymol.* **326**, 245–254. https://doi.org/10.1016/S0076-6879(00)26058-8.

[19]. Kaufmann, M., Lindner, P., Honegger, A., Blank, K., Tschopp, M., Capitani, G., et al., (2002). Crystal structure of the anti-His tag antibody 3D5 single-chain fragment complexed to its antigen. *J. Mol. Biol.* **318**, 135–147. https://doi.org/10.1016/S0022-2836(02)00038-4.

[20]. Asano, T., Takei, J., Furusawa, Y., Saito, M., Suzuki, H., Kaneko, M.K., et al., (2021). Epitope mapping of an anti-CD20 monoclonal antibody (C(20)Mab-60) using the HisMAP method. *Monoclon. Antib. Immunodiagn. Immunother.* **40**, 243–249. https://doi.org/10.1089/mab.2021.0035.

[21]. Jurrus, E, Engel, D, Star, K, Monson, K, Brandi, J, Felberg, LE, et al., (2018). Improvements to the APBS biomolecular solvation software suite. *Protein Sci* **27**, 112–128. https://doi.org/10.1002/pro.3280.

[22]. Arimori, T., Kitago, Y., Umitsu, M., Fujii, Y., Asaki, R., Tamura-Kawakami, K., et al., (2017). Fv-clasp: an artificially designed small antibody fragment with improved production compatibility, stability, and crystallizability. *Structure* **25**, 1611–1622.e4. https://doi.org/10.1016/j.str.2017.08.011.

[23]. Krissinel, E., Henrick, K., (2007). Inference of macromolecular assemblies from crystalline state. *J. Mol. Biol.* **372**, 774–797. https://doi.org/10.1016/j.jmb.2007.05.022.

[24]. Schmitt, J., Hess, H., Stunnenberg, H.G., (1993). Affinity purification of histidine-tagged proteins. *Mol. Biol. Rep.* **18**, 223–230. https://doi.org/10.1007/bf01674434.

[25]. Rini, J.M., Schulze-Gahmen, U., Wilson, I.A., (1992). Structural evidence for induced fit as a mechanism for antibody-antigen recognition. *Science* **255**, 959–965. https://doi.org/10.1126/science.1546293.

[26]. Churchill, M.E., Stura, E.A., Pinilla, C., Appel, J.R., Houghten, R.A., Kono, D.H., et al., (1994). Crystal

structure of a peptide complex of anti-influenza peptide antibody Fab 26/9. Comparison of two different antibodies bound to the same peptide antigen. *J. Mol. Biol.* **241**, 534–556. https://doi.org/10.1006/jmbi.1994.1530.

[27]. Krauss, N., Wessner, H., Welfle, K., Welfle, H., Scholz, C., Seifert, M., et al., (2008). The structure of the anti-c-myc antibody 9E10 Fab fragment/epitope peptide complex reveals a novel binding mode dominated by the heavy chain hypervariable loops. *Proteins* **73**, 552–565. https://doi.org/10.1002/prot.22080.

[28]. Beugelink, J.W., Sweep, E., Janssen, B.J.C., Snijder, J., Pronker, M.F., (2024). Structural basis for recognition of the FLAG-tag by anti-FLAG M2. *J. Mol. Biol.* **436**, 168649. https://doi.org/10.1016/j.jmb.2024.168649.

[29]. Fujii, Y., Matsunaga, Y., Arimori, T., Kitago, Y., Ogasawara, S., Kaneko, M., et al., (2016). Tailored placement of a turn-forming PA tag into the structured domain of a protein to probe its conformational state. *J. Cell Sci.*, 1512–1522. https://doi.org/10.1242/jcs.176685.

[30]. Ji, W., Miao, A., Liang, K., Liu, J., Qi, Y., Zhou, Y., et al., (2024). Substrate binding and inhibition mechanism of norepinephrine transporter. *Nature* **633**, 473–479. https://doi.org/10.1038/s41586-024-07810-5.

[31]. Wiseman, T., Williston, S., Brandts, J.F., Lin, L.N., (1989). Rapid measurement of binding constants and heats of binding using a new titration calorimeter. *Anal. Biochem.* **179**, 131–137. https://doi.org/10.1016/0003-2697(89)90213-3.

[32]. Kato, R., Hiraki, M., Yamada, Y., Tanabe, M., Senda, T., (2021). A fully automated crystallization apparatus for small protein quantities. *Acta Crystallogr. F Struct. Biol. Commun.* **77**, 29–36. https://doi.org/10.1107/S2053230X20015514.

[33]. Kabsch, W., (2010). Xds. *Acta Crystallogr. D Biol. Crystallogr.* **66**, 125–132. https://doi.org/10.1107/S0907444909047337.

[34]. Mccoy, A.J., Grosse-Kunstleve, R.W., Adams, P.D., Winn, M.D., Storoni, L.C., Read, R.J., (2007). Phaser crystallographic software. *J. Appl. Cryst.* **40**, 658–674. https://doi.org/10.1107/S0021889807021206.

[35]. Adams, P.D., Afonine, P.V., Bunkoczi, G., Chen, V.B., Davis, I.W., Echols, N., et al., (2010). PHENIX: a comprehensive Python-based system for macromolecular structure solution. *Acta Crystallogr. D Biol. Crystallogr.* **66**, 213–221. https://doi.org/10.1107/S0907444909052925.

[36]. Emsley, P., Cowtan, K., (2004). Coot: model-building tools for molecular graphics. *Acta Crystallogr. D Biol. Crystallogr.* **60**, 2126–2132. https://doi.org/10.1107/S0907444904019158.

[37]. Chen, V.B., Arendall, W.B., Headd, J.J., Keedy, D.A., Immormino, R.M., Kapral, G.J., et al., (2010). MolProbity: all-atom structure validation for macromolecular crystallography. *Acta Crystallogr. D Biol. Crystallogr.* **66**, 12–21. https://doi.org/10.1107/S0907444909042073.

[38]. Mastronarde, D.N., (2005). Automated electron microscope tomography using robust prediction of specimen movements. *J. Struct. Biol.* **152**, 36–51. https://doi.org/10.1016/j.jsb.2005.07.007.

[39]. Zheng, S.Q., Palovcak, E., Armache, J.P., Verba, K.A., Cheng, Y., Agard, D.A., (2017). MotionCor2: anisotropic correction of beam-induced motion for improved cryo-electron microscopy. *Nature Methods* **14**, 331–332. https://doi.org/10.1038/nmeth.4193.

[40]. Rohou, A., Grigorieff, N., (2015). CTFFIND4: fast and accurate defocus estimation from electron micrographs. *J. Struct. Biol.* **192**, 216–221. https://doi.org/10.1016/j.jsb.2015.08.008.

[41]. Kimanius, D., Dong, L., Sharov, G., Nakane, T., Scheres, S.H.W., (2021). New tools for automated cryo-EM single-particle analysis in RELION-4.0. *Biochem. J.* **478**, 4169–4185. https://doi.org/10.1042/BCJ20210708.

[42]. Jumper, J., Evans, R., Pritzel, A., Green, T., Figurnov, M., Ronneberger, O., et al., (2021). Highly accurate protein structure prediction with AlphaFold. *Nature* **596**, 583–589. https://doi.org/10.1038/s41586-021-03819-2.

[43]. Pettersen, E.F., Goddard, T.D., Huang, C.C., Meng, E.C., Couch, G.S., Croll, T.I., et al., (2021). UCSF ChimeraX: structure visualization for researchers, educators, and developers. *Protein Sci.* **30**, 70–82. https://doi.org/10.1002/pro.3943.